# Generalized inverse lithography methods for phase-shifting mask design

**Xu Ma**[a] **and Gonzalo R. Arce**[b]
*Department of Electrical and Computer Engineering, University of Delaware, Newark, DE, 19716, U.S.A.*
[a]maxu@udel.edu and [b]arce@ece.udel.edu

**Abstract:** Optical proximity correction (OPC) and phase shifting masks (PSM) are resolution enhancement techniques (RET) used extensively in the semiconductor industry to improve the resolution and pattern fidelity of optical lithography. In this paper, we develop generalized gradient-based RET optimization methods to solve for the inverse lithography problem, where the search space is not constrained to a finite phase tessellation but where arbitrary search trajectories in the complex space are allowed. Subsequent mask quantization leads to efficient design of PSMs having an arbitrary number of discrete phases. In order to influence the solution patterns to have more desirable manufacturability properties, a wavelet regularization framework is introduced offering more localized flexibility than total-variation regularization methods traditionally employed in inverse problems. The proposed algorithms provide highly effective four-phase PSMs capable of generating mask patterns with arbitrary Manhattan geometries. Furthermore, a double-exposure optimization method for general inverse lithography is developed where each exposure uses an optimized two-phase mask.

© 2007 Optical Society of America

**OCIS codes:** (220.3740) Lithography; (100.3190) Inverse problems; (100.7410) Wavelets; (050.5080) Phase shift.

## References and links

1. S. V. G. J. Schneider, J. Murakowski and D. W. Prather, "Combination lithography for photoniccrystal circuits," of Vacuum Science and Technology B **22(1)**, 146–151 (2004).
2. J. M. M. J. M. P. Yao, G. J. Schneider and D. W. Prather, "Micro/nano lithography realized by chemical printing," in *Proceedings of SPIE - The International Society for Optical Engineering*, vol. 6151I of *Emerging Lithographic Technologies X*, p. 61511N (2006).
3. D. W. P. E. D. W. P. Yao, G. J. Schneider and D. J. O'Brien, "Fabrication of three-dimensional photonic crystals with multilayer photolithography," Optics Express **13**, 2370–2376 (2005).
4. B. L. M. J. M. D. W. P. E. D. W. P. Yao, G. J. Schneider and D. J. O'Brien, "Multilayer three-dimensional photolithography with traditional planar method," Applied Physics Letters **85**, 2920–2922 (2004).
5. A. K. Wong, *Resolution enhancement techniques*, vol. 1 (SPIE Press, 2001).
6. S. A. Campbell, *The science and engineering of microelectronic fabrication*, 2nd ed. (Publishing House of Electronics Industry, 2003).
7. F. Schellenberg, "Resolution enhancement technology: The past, the present, and extensions for the future, Optical Microlithography," Proc. SPIE **5377**, 1–20 (2004).
8. F. Schellenberg, *Resolution enhancement techniques in optical lithography* (SPIE Press, 2004).
9. A. W. M. L. W. L. L. Liebmann, S. Mansfield and T. Dunham, "TCAD development for lithography resolution enhancement," IBM Journal of Research and Development pp. 651–665 (2001).
10. N. S. V. M. D. Levenson and R. A. Simpson, "Improving resolution in photolithography with a phase-shifting mask," IEEE Trans. Electron Devices **ED-29**, 1828–1836 (1982).

#86458 - $15.00 USD Received 15 Aug 2007; revised 21 Sep 2007; accepted 26 Oct 2007; published 31 Oct 2007

11. B. S. S. Sherif and R. Leone, “Binary image synthesis using mixed integer programming,” IEEE Transactions on Image Processing **4**(9), 1252–1257 (1995).
12. Y. Liu and A. Zakhor, “Binary and phase shifting mask design for optical lithography,” IEEE Transactions on Semiconductor Manufacturing **5**(2) (1992).
13. Y. C. Pati and T. Kailath, “Phase-shifting masks for microlithography: Automated design and mask requirements,” Optical Society of America **11** (1994).
14. T. F. B. T. A. Erdmann, R. Farkas and G. Kokai, “Towards automatic mask and source optimization for optical lithography,” Optical Microlithography, Proc. SPIE **5377**, 646–657 (2004).
15. Y. L. L. Pang and D. Abrams, “Inverse lithography technology (ILT): What is the impact to the photomask industry?” Proc. SPIE (2006).
16. Y. Granik, “Illuminator optimization methods in microlithography,” Optical Microlithography Proc. SPIE **5754**, 217–229 (2005).
17. A. Poonawala and P. Milanfar, “OPC and PSM design using inverse lithography: A non-linear optimization approach,” in *Proceedings of the SPIE*, vol. 6154, pp. 1159–1172 (San Jose, CA, 2006).
18. C. Vogel, *Computational methods for inverse problems* (SIAM Press, 2002).
19. X. Ma and G. R. Arce, “Generalized inverse lithography methods for phase-shifting mask design,” in *Proceedings of SPIE*, vol. 65200U (2007).
20. A. Poonawala and P. Milanfar, “Double Exposure Mask Synthesis using Inverse Lithography,” submitted to Journal of Microlithography, Microfabrication, and Microsystems .
21. M. Born and E. Wolfe, *Principles of optics* (Cambridge University Press, 1999).
22. N. Cobb and A. Zakhor, “Fast sparse aerial image calculation for OPC,” BACUS Symposium on Photomask Technology, Proc. SPIE **2440**, 313–327 (1995).


---

## 1. Introduction

Due to resolution limits of optical lithographic systems, the electronics and photonics industry have relied on 2D and 3D resolution enhancement techniques (RET) to compensate and minimize mask distortions as they are projected onto semiconductor wafers [1, 4, 5]. Resolution in optical lithography obeys the Rayleigh criterion $resolution(R) = k\frac{\lambda}{NA}$, where $\lambda$ is the wavelength, $NA$ is the numerical aperture taking on values around 0.9 for most lithography systems used today, and $k$ is the process constant which can be minimized through RET methods [6, 7, 8, 9]. RET methods manipulate the local amplitude and phase features of the optical wavefront to pre-compensate for imaging distortions. Optical and process correction (OPC) methods modify the mask amplitude by the addition of sub-resolution features to the mask pattern [5]. Phase shifting masks (PSMs), commonly attributed to Levenson [10], induce phase shifts in the transmitted field which has a favorable constructive or destructive interference effect. Thus, a suitable modulation of both the phase and the intensity of the incident light can be used to effectively compensate for some of the resolution-limiting phenomena in optical diffraction. The challenge is then to develop a general systematic method to design pre-compensated masks also referred to as inverse lithography technology (ILT).

Several approaches to inverse lithography have been proposed in the literature. These range from heuristic and empirically-based design rules to computationally expensive optimization-based inverse algorithms. Sherif, et al. derived an iterative approach to generate binary masks [11]. Liu and Zakhor developed a binary and phase shifting mask design strategy based on the branch and bound algorithm and simulated annealing [12]. Pati-Kailath exploited a class of approximations for partially coherent imaging systems to develop sub-optimal projections onto convex sets for PSM designs [13]. In addition, Erdmann proposed automatic optimization of the mask and illumination parameters with a genetic algorithm [14]. Pang, et al. gave an overview of ILT and provided some simulations to demonstrate the benefit of ILT [15]. Granik described and compared solutions of inverse mask problems [16]. All of the methods mentioned above, however, are not based on gradient type optimization and thus the searching process for a suitable solution is either computationally expensive or not efficient. Recently, Poonawala and Milanfar introduced a novel optimization framework for inverse lithography based on a pixel-based, continuous function formulation, well suited for gradient-based search [**?**, 17].

#86458 - $15.00 USD Received 15 Aug 2007; revised 21 Sep 2007; accepted 26 Oct 2007; published 31 Oct 2007
(C) 2007 OSA

Based on a steepest descent search, this approach exploits the rich theory of regularized iterative optimization [18].

Letting $M(x,y)$ be the input mask to an optical lithography system $T\{\cdot\}$, approximated as a low-pass spatial filter followed by a soft threshold operation, the output pattern is denoted as $Z(x,y) = T\{M(x,y)\}$. Given a $N \times N$ desired output pattern $Z^*(x,y)$, the goal of PSM design is to find the optimized $M(x,y)$ called $\hat{M}(x,y)$ such that the distance $D = d(Z(x,y), Z^*(x,y)) = d(T\{M(x,y)\}, Z^*(x,y))$ is minimized, where $d(\cdot,\cdot)$ is the mean square error criterion. The PSM inverse lithography optimization problem can thus be formulated as the search of $\hat{M}(x,y)$ over the $N \times N$ complex space $C^{N\times N}$ such that

$$\hat{M}(x,y) = arg \min_{M(x,y)\in C^{N\times N}} d(T\{M(x,y)\}, Z^*(x,y)). \quad (1)$$

With the goal of attaining two-phase-level optimized masks, the system in Ref. [17] further constrained $M(x,y)$ in Eq. (1) such that $M(x,y) = cos(\theta(x,y))$, thus searching over the range of $\theta$ and thus constraining the value of $M$ in the interval $M(x,y) \in (-1,1)$ and in essence representing masks limited to two phases. While this approach is very effective in some cases, the end result is that the search generally fails to generate adequate PSM for mask patterns having arbitrary Manhattan geometries [19]. According to the "Four-Phase Theorem" described in Ref. [13], given an arbitrary pattern with a Manhattan geometry, a phase-shifting mask used to synthesize the image pattern must use a minimum of four distinct phase levels.

The main goal of this paper is thus to overcome this limitation of the Poonawala, et al. algorithm in Ref. [17], so as to obtain a generalized synthesis algorithm capable of generating arbitrary mask patterns. This is accomplished as follows: First, the iterative optimization framework is re-formulated where the search trajectory is unconstrained in the complex plane. The optimization problem is thus broadly formulated as in Eq. (1). As expected, the resultant mask patterns obtained by Eq. (1) have arbitrary complex pixel values, and consequently a post-processing step is used to quantize the patterns into the desired four-phase-level, shifting-mask patterns.

A second contribution of the paper is the introduction of a new regularization framework. Inverse lithography is an ill-posed problem where numerous input patterns can lead to the same binary output pattern. Regularization in ILT seeks to bias the solution space to sample solutions that have lower manufacturabilty complexity. We introduce an effective detail-reduction approach referred to as "wavelet penalty" regularization.

Finally, in the event that four-phase masks are difficult to fabricate, but the goal is to still synthesize masks with arbitrary geometry, a third contribution of the paper is the development of a double-exposure PSM optimization method, where at each stage the PSM masks are constrained to have two phases. The two-stage exposure method can lead to high fidelity output pattern reproduction at the expense of a more complex exposure process. Poonawala and Milanfar, independently from our work, have simultaneously developed a different double-exposure method [20].

## 2. PSM design and problem formulation

The methods developed in this paper extend and generalize the model and approach proposed in Ref. [17], illustrated in Fig. 1. The complex-valued mask is the input of the system, where the phase pattern of the propagating light is modified by a phase shifting material overcoating the mask. Light propagating through the mask pattern is affected by diffraction and mutual interference—a phenomena described by the Hopkins Diffraction Model [21, 22]. The light that transmitted through the mask reaches a light-sensitive photoresist, which is subsequently developed through the use of solvents. The thickness of the remaining photoresist after development is proportional to the exposure dose exceeding a given threshold intensity. In a positive

#86458 - $15.00 USD Received 15 Aug 2007; revised 21 Sep 2007; accepted 26 Oct 2007; published 31 Oct 2007
(C) 2007 OSA

photoresist process, almost all the photoresist material remains in the low-exposure area on the wafer and is removed in the high-exposure area. Between these two extremes is the transition region. For mathematical simplicity, it is assumed that when the light field exceeds a threshold, the exposed area becomes a high-exposure area, otherwise, a low-exposure area. Thus, a hard threshold operation can adequately represent the exposure effect described above and the output pattern of the optical system is binary. This is an approximate model for the field transfering through the mask. In Fig. 1, $|\cdot|$ is the element-by-element absolute operation. In this paper,

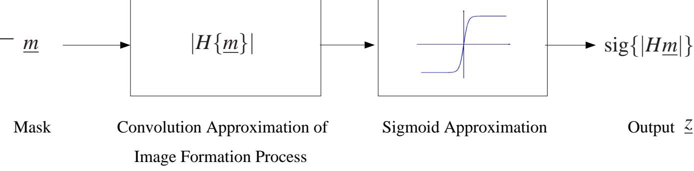


Fig. 1. Approximated forward process model. (Ref. [17], Fig. 1).

only coherent imaging is considered, and the aerial image formation process is approximated by a convolution between the mask pattern and a Gaussian low pass filter $h$. In the pixel-based algorithm, $pixel\ size = resolution(R) = k\frac{\lambda}{NA}$. The standard deviation of the Gaussian low-pass filter $h$ is $\sigma = \frac{R\times NA}{\lambda} = k$. The output of the convolution and the absolute operation model is the electrical field amplification distribution of the aerial image. Further, since the derivative of the sigmoid function exists, it is used to approximate the hard threshold function. The hard threshold function is a shifted unit step function $U(x-t_r)$, which is approximated by the sigmoid function

$$\mathrm{sig}(x) = \frac{1}{1+\exp[-a(x-t_r)]}, \tag{2}$$

where $t_r$ is the process threshold, and $a$ dictates the steepness of the sigmoid function.

The mask is represented by an $M_{N\times N}$ matrix with a $N^2\times 1$ equivalent raster scanned vector representation $\underline{m}_{N^2\times 1}$ which is denoted as $\underline{m}$ for short notation. Following the definitions above, the following notation is used:

1) A convolution matrix H is a $N^2\times N^2$ matrix denoting an equivalent two-dimensional low-pass filter $h$.

2) The desired $N\times N$ binary output pattern is denoted as $Z^*$. It is the desired light distribution sought on the wafer. Its vector representation is denoted as $\underline{z}^*$.

3) The output of the sigmoid function is the $N\times N$ real-valued image denoted as $Z = sig\{|H\{M\}|\}$. The equivalent vector is denoted as $\underline{z}\in\Re^{N^2\times 1}$.

4) The hard threshold version of $Z$ is the binary output pattern denoted as $Z_b$. Its equivalent vector is denoted as $\underline{z}_b\in\Re^{N^2\times 1}$, with all entries constrained to 0 or 1.

5) The electrical field of the input mask is denoted as the complex-valued $N\times N$ matrix $M$ and it is equivalently represented as $\underline{m}\in C^{N^2\times 1}$, where $C^{N^2\times 1}$ is the set of $N^2\times 1$ complex vector. All entries in $M$ and $\underline{m}$ can take on unrestricted complex values.

6) The pole-constrained mask $M_p$ is the quantization of $M$. The pixel magnitudes of $M_p$ are quantized to 0 or 1. The pixel phases are quantized to several discrete phase levels. Its equivalent vector is denoted as $\underline{m}_p\in C^{N^2\times 1}$.

7) The optimized $N\times N$ complex-valued mask denoted as $\hat{M}$ minimizes the distance between $Z$ and $Z^*$, ie,

$$\hat{M} = arg\min_{M} d(\mathrm{sig}\{|H\{M\}|\}, Z^*). \tag{3}$$

Its equivalent vector is denoted as $\hat{\underline{m}}\in C^{N^2\times 1}$.

#86458 - $15.00 USD Received 15 Aug 2007; revised 21 Sep 2007; accepted 26 Oct 2007; published 31 Oct 2007
(C) 2007 OSA

8) The pole-constrained optimized mask $\hat{M}_p$ is the quantization of $\hat{M}$. Its equivalent vector is denoted as $\underline{\hat{m}}_p \in C^{N^2\times 1}$.

Given the gray level pattern $\underline{z} = \mathrm{sig}\{|H\{\underline{m}\}|\}$, the $ith$ entry in this vector can be represented as

$$\underline{z}_i = \frac{1}{1+\exp[-a|\sum_{j=1}^{N^2} h_{ij}\underline{m}_j| + at_r]}, \quad i = 1,\ldots N^2, \tag{4}$$

where $h_{ij}$ is the $i,jth$ entry of the filter. In the optimization process, $\underline{\hat{m}}$ is searched to minimize the $L_2$ norm of the difference between $\underline{z}$ and $\underline{z}^*$. Therefore, $\underline{\hat{m}} = arg\min_{\underline{\hat{m}}}\{F(\underline{m})\}$, where the cost function $F(\cdot)$ is defined as:

$$F(\underline{m}) = \|\underline{z}^* - \underline{z}\|_2^2 = \sum_{i=1}^{N^2}(z_i^* - z_i)^2 = \sum_{i=1}^{N^2}(z_i^* - \frac{1}{1+\exp[-a|\sum_{j=1}^{N^2} h_{ij}\underline{m}_j| + at_r]})^2. \tag{5}$$

## 3. Generalized PSM design algorithm

As stated before, two-phase-level PSMs are not adequate to generate arbitrary patterns with Manhattan geometries [13] and phase conflicts are likely to arise. According to the $Four-Phase\ Theorem$ [13], the number of discrete phase levels used in PSM design should be at least four, in order to avoid conflicts and ambiguities in the assignment of phases. The inverse model-based algorithms in Ref. [17] is not suited for optimization of masks having more than two-phase levels (0 and $\pi$). This drawback motivates us to develop a generalized algorithm, admitting an arbitrary number of discrete phase levels, which overcomes this limitation.

Let $\underline{r}$ and $\underline{\theta}$ be the magnitude and phase components of the complex-valued mask

$$\underline{m}_k = \underline{r}_k e^{j\underline{\theta}_k}, \quad k = 1,\ldots,N^2, \tag{6}$$

where $j = \sqrt{-1}$, $\underline{\theta}_k \in (-\infty,\infty)$ and $\underline{r}_k \in [0,1]$. The bound-constrained optimization is then reduced to an unconstrained optimization problem using following parametric transformation,

$$\underline{r}_k = \frac{1+\cos\underline{\phi}_k}{2}, \quad k = 1,\ldots,N^2, \tag{7}$$

where $\underline{\phi}_k \in (-\infty,\infty)$. Substituting $\underline{r}_k$ in Eq. (6) with Eq. (7), we have,

$$\underline{m}_k = \frac{1+\cos\underline{\phi}_k}{2} e^{j\underline{\theta}_k}, \quad k = 1,\ldots,N^2. \tag{8}$$

Defining the vector $\underline{\theta} = [\theta_1,\ldots,\theta_{N^2}]^T$ and $\underline{\phi} = [\phi_1,\ldots,\phi_{N^2}]^T$, the optimization problem is formulated as:

$$(\underline{\hat{\theta}},\underline{\hat{\phi}}) = arg\min_{(\underline{\theta},\underline{\phi})}\{F(\underline{\theta},\underline{\phi})\}, \tag{9}$$

where the cost function is:

$$\begin{aligned} F(\underline{\theta},\underline{\phi}) &= \|\underline{z}^* - \underline{z}\|_2^2 = \sum_{i=1}^{N^2}(z_i^* - z_i)^2 \\ &= \sum_{i=1}^{N^2}\left(z_i^* - \frac{1}{1+\exp[-a\sqrt{(\sum_{k=1}^{N^2} h_{ik}\frac{1+\cos\underline{\phi}_k}{2}e^{j\underline{\theta}_k})^2} + at_r]}\right)^2. \end{aligned} \tag{10}$$

#86458 - $15.00 USD Received 15 Aug 2007; revised 21 Sep 2007; accepted 26 Oct 2007; published 31 Oct 2007
(C) 2007 OSA

The steepest-descent method is used to optimize the above problem. The gradients $\nabla F(\underline{\theta},\underline{\phi})_{\underline{\theta}}$ and $\nabla F(\underline{\theta},\underline{\phi})_{\underline{\phi}}$ can be calculated as follows [19]:

$$\begin{aligned}\nabla F(\underline{\theta},\underline{\phi})_{\underline{\theta}} = \underline{d}_{\underline{\theta}} &= 2a\times\frac{\mathbf{\underline{1}}+\cos\underline{\phi}}{2}\odot\sin\underline{\theta}\odot\{H^T[(\underline{z}^*-\underline{z})\odot\underline{z}\odot(\mathbf{\underline{1}}-\underline{z})\odot H(\underline{m}_R)\odot T(\underline{m})]\}\\ &- 2a\times\frac{\mathbf{\underline{1}}+\cos\underline{\phi}}{2}\odot\cos\underline{\theta}\odot\{H^T[(\underline{z}^*-\underline{z})\odot\underline{z}\odot(\mathbf{\underline{1}}-\underline{z})\odot H(\underline{m}_I)\odot T(\underline{m})]\},\end{aligned} \tag{11}$$

$$\begin{aligned}\nabla F(\underline{\theta},\underline{\phi})_{\underline{\phi}} = \underline{d}_{\underline{\phi}} &= a\times\sin\underline{\phi}\odot\cos\underline{\theta}\odot\{H^T[(\underline{z}^*-\underline{z})\odot\underline{z}\odot(\mathbf{\underline{1}}-\underline{z})\odot H(\underline{m}_R)\odot T(\underline{m})]\}\\ &+ a\times\sin\underline{\phi}\odot\sin\underline{\theta}\odot\{H^T[(\underline{z}^*-\underline{z})\odot\underline{z}\odot(\mathbf{\underline{1}}-\underline{z})\odot H(\underline{m}_I)\odot T(\underline{m})]\},\end{aligned} \tag{12}$$

where $\nabla F(\underline{\theta}) \in \Re^{N^2\times 1}$, $\odot$ is the element-by-element multiplication operator, and $T(\underline{m}) = [H(\underline{m}_R)^2+H(\underline{m}_I)^2]^{-\frac{1}{2}}$. $\underline{m}_R$ and $\underline{m}_I$ are the real part and the imaginary part of $\underline{m}$. $\mathbf{\underline{1}} = [1,\ldots,1]^T \in \Re^{N^2\times 1}$. Assuming $\underline{\theta}^k$ and $\underline{\phi}^k$ are the $k^{th}$ iteration results, then at the $k+1^{th}$ iteration:

$$\underline{\theta}^{k+1} = \underline{\theta}^k - s_{\underline{\theta}}\underline{d}^k_{\underline{\theta}}, \tag{13}$$

$$\underline{\phi}^{k+1} = \underline{\phi}^k - s_{\underline{\phi}}\underline{d}^k_{\underline{\phi}}, \tag{14}$$

where $s_{\underline{\theta}}$ and $s_{\underline{\phi}}$ are the step-sizes. The iterative optimization above, in general, leads to complex-valued solutions that are not constrained to a discrete number of magnitude and phase levels. Therefore a post-processing step is needed to obtain the pole-constrained optimized mask, $\underline{\hat{m}}_p$. Since $\underline{\hat{m}}$ is complex-valued, a two-step quantization process is followed. First the magnitudes are quantized by a global threshold $t_m$ as $|\underline{\hat{m}}_{pi}| = U(|\underline{\hat{m}}_i| - t_m)$, where $i = 1,\ldots,N^2$. The phases are subsequently quantized to the nearest prescribed discrete phase level. We define the pattern error $E$ as the distance between the desired output pattern $Z^*$ and the actual binary output pattern $Z_b$:

$$E = \sum_{i=1}^{N^2} |\underline{z}_i^* - \underline{z}_{bi}| = \sum_{i=1}^{N^2} |\underline{z}_i^* - \Gamma|H\underline{m}_{pi}||. \tag{15}$$

When the pattern error is reduced to a tolerable level, the steepest descent iteration is stopped.

In order to demonstrate the effect of the number of phases used in PSM design, consider the desired pattern shown in Fig. 2. The top horizontal block cross-connects two vertical parallel blocks. The phases assigned to the two parallel adjacent blocks cannot be the same, so as to exploit the PSM principle. Since the horizontal top block connects the parallel blocks, and since it would be desirable that there are no gaps introduced in the image, the horizontal block must be assigned an intermediate phase value that is distinct from the phases of the two parallel blocks. Therefore, two-phase levels are not sufficient to attain this goal. The conflict can be eliminated with the use of four phases. In Fig. 2, the patterns in the top row and the middle row illustrate the input patterns. The output patterns are shown in the bottom row. The three images in the bottom row show the output patterns of (left) the desired pattern ($\underline{z}^*$), (center) the complex-valued optimized mask ($\underline{\hat{m}}$), and (right) the pole-constrained optimized mask ($\underline{\hat{m}}_p$). The aerial image formation process is approximated by a $11\times 11$ Gaussian low pass filter with $k = 14$, in the sigmoid function, we assign parameters $a = 80$ and $t_r = 0.5$. The global threshold is $t_m = 0.5$. The shape of the image used to initialize the iterative algorithm is the same as

#86458 - $15.00 USD Received 15 Aug 2007; revised 21 Sep 2007; accepted 26 Oct 2007; published 31 Oct 2007
(C) 2007 OSA

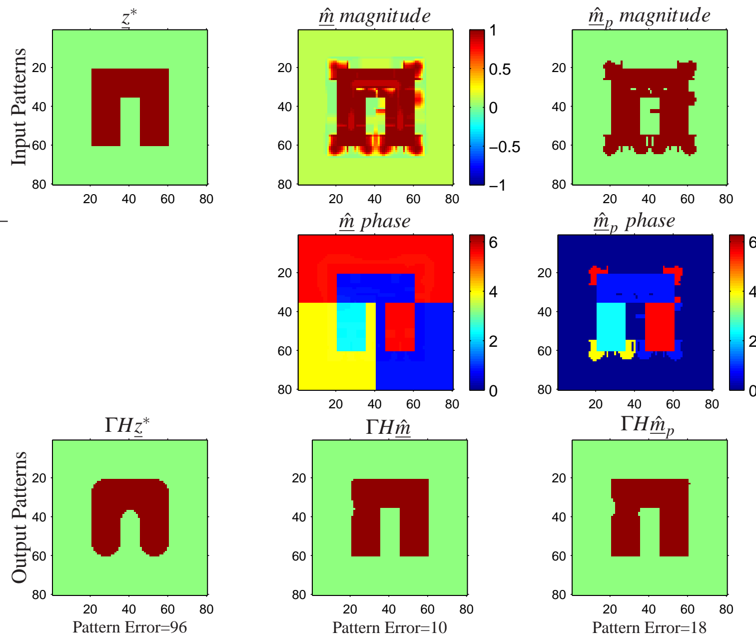


Fig. 2. Top row (input masks), left to right: desired pattern, magnitude of the optimized complex-valued mask and optimized pole-constrained mask obtained using a threshold $t_m$. The middle row indicates the phases of the optimized complex-valued mask. The bottom row indicates the corresponding binary output patterns. The parameters used in the simulation are $a = 80$, $t_r = 0.5$, $t_m = 0.5$, $11 \times 11$ Gaussian low pass filter with $k = 14$, $s_{\underline{\phi}} = 2$ and $s_{\underline{\theta}} = 0.01$. Green, red and blue represent 0, 1 and -1 respectively in the top and bottom rows; Dark blue, light blue, yellow and red represent $\frac{\pi}{4}$, $\frac{3\pi}{4}$, $\frac{5\pi}{4}$ and $\frac{7\pi}{4}$ respectively in the middle row.

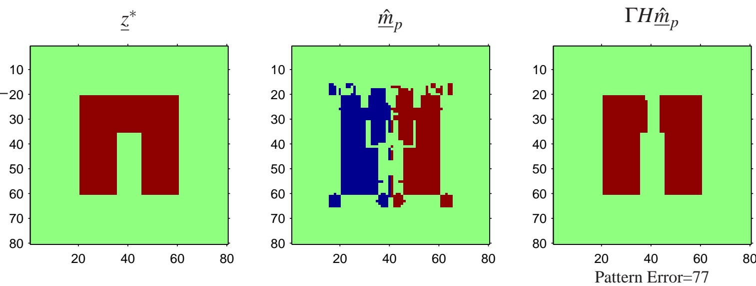


Fig. 3. Left to right: desired pattern, pole-constraied optimized mask and binary output pattern. $s_{\underline{\phi}} = 2$, $s_{\underline{\theta}} = 0.01$. Red and blue represent 0 and $\pi$ phases respectively.

#86458 - $15.00 USD Received 15 Aug 2007; revised 21 Sep 2007; accepted 26 Oct 2007; published 31 Oct 2007
(C) 2007 OSA

the desired binary output pattern $Z^*$. For $\underline{\phi}_k$, we assign the phase of $\frac{\pi}{5}$ corresponding to the areas having a magnitude of 1 and a phase of $\frac{4\pi}{5}$ for the areas with magnitude of 0. The phase assignment must be done a-priori and phases in neighboring blocks are assigned alternately. Because of the numerous *sine* and *cosine* functions in Eq. (11) and Eq. (12), we intentionally avoid assigning $\underline{\theta}_k$ and $\underline{\phi}_k$ the values of 0, $\frac{\pi}{2}$, $\pi$ or $\frac{3\pi}{2}$. Otherwise, Eq. (11) or Eq. (12) may reduce to a zero update, terminating the iteration. For a four-phase-level mask design, empirical observations show that an efficient assignment of phase values to $\underline{\theta}_k$ is to select phases in the set of $\frac{\pi}{4}$, $\frac{3\pi}{4}$, $\frac{5\pi}{4}$ and $\frac{7\pi}{4}$. Further, regions around a block should be assigned a phase value that is $\frac{\pi}{2}$ different from that of the block and on the same side of the imaginary axis. This approach has proved efficient in our extensive simulation analysis. As a comparison to the four-phase PSM design, the experiment using just two phases is illustrated in Fig. 3. Note that a gap appears on the top connection of the synthesized mask, as expected.

## 4. Regularization

As illustrated in Fig. 2, the optimized mask patterns contain numerous details, which may bring difficulty to mask fabrication. Most of the details consist of singular transmission pixels. One approach to reduce image detail is through regularization during the optimization process [18, 17]. Regularization is formulated as follows:

$$\hat{\underline{m}} = arg \min_{\hat{\underline{m}}} \{F(\underline{m}) + \gamma R(\underline{m})\}, \tag{16}$$

where $F(\underline{m})$ is the data-fidelity term and $R(\underline{m})$ is the regularization term which is used to reduce the solution space and constrain the optimized results. $\gamma$ is the user-defined parameter to reveal the weight of the regularization. In the following, we will discuss pole penalty and the wavelet penalty.

### *4.1. Pole penalty*

The pole penalty is used to constrain the magnitude and phase of each pixel value in the optimized mask to several prescribed discrete levels, so the pole penalty is divided into the magnitude pole penalty and the phase pole penalty. Poonawala and Milanfar used the pole penalty approach favoring a two-phase-level solution. In order to extend the pole-penalty method to the algorithm developed in Section 3, it is generalized to admit an arbitrary number of phase levels.

The magnitude pole-penalty term is:

$$R_{pole}(\underline{m}) = \sum_{i=1}^{N^2} \underline{|m|}_i^2 = \underline{|m|}^T \underline{|m|}. \tag{17}$$

For each pixel value, the corresponding penalty is the quadratic function $r(\underline{m}_i) = \underline{|m|}_i^2, \quad i = 1,\ldots,N^2$. According to Eq. (17), the gradient of $R_{pole}(\underline{m})$ is $\nabla R_{pole}(\underline{m}) = 2\underline{|m|}$, thus, the cost function in Eq. (5) is adjusted as $J(\underline{m}) = F(\underline{m}) + \gamma_{pole} R_{pole}(\underline{m})$. In the phase penalty, the phases are constrained to the closest phase levels. If we use two-phase levels, the regularization term is:

$$R_{pole}(\underline{\theta}) = \sum_{i=1}^{N^2} [\sin(2\underline{\theta}_i - \frac{\pi}{2}) + 1]^2 = [\sin(2\underline{\theta} - \frac{\pi}{2}) + \underline{\mathbf{1}}]^T [\sin(2\underline{\theta} - \frac{\pi}{2}) + \underline{\mathbf{1}}]. \tag{18}$$

For each pixel value, the corresponding penalty depicted by solid line in Fig. 4 is $r(\underline{\theta}_i) = [\sin(2\underline{\theta}_i - \frac{\pi}{2}) + 1]^2, \quad i = 1,\ldots,N^2$. According to Eq. (18), the gradient of $R_{pole}(\underline{\theta})$ is:

$$\nabla R_{pole}(\underline{\theta}) = 4[\sin(2\underline{\theta} - \frac{\pi}{2}) + \underline{\mathbf{1}}]^T \cos(2\underline{\theta} - \frac{\pi}{2}). \tag{19}$$

#86458 - $15.00 USD Received 15 Aug 2007; revised 21 Sep 2007; accepted 26 Oct 2007; published 31 Oct 2007
(C) 2007 OSA

If four-phase levels are considered, the regularization term is then obtained as:

$$R_{pole}(\underline{\theta}) = \sum_{i=1}^{N^2}[\sin(4\underline{\theta}_i - \frac{3\pi}{2}) + 1]^2 = [\sin(4\underline{\theta}_i - \frac{3\pi}{2}) + \mathbf{\underline{1}}]^T[\sin(4\underline{\theta}_i - \frac{3\pi}{2}) + \mathbf{\underline{1}}]. \tag{20}$$

For each pixel value, the corresponding penalty depicted by the dash-dot line in Fig. 4 is:

$$r(\underline{\theta}_i) = [\sin(4\underline{\theta}_i - \frac{3\pi}{2}) + 1]^2, \quad i = 1, \ldots, N^2 \tag{21}$$

and the gradient of $R_{pole}(\underline{\theta})$ is:

$$\nabla R_{pole}(\underline{\theta}) = 8[\sin(4\underline{\theta} - \frac{3\pi}{2}) + \mathbf{\underline{1}}]^T \cos(4\underline{\theta} - \frac{3\pi}{2}). \tag{22}$$

Using the pole penalty described in Eq. (17) and Eq. (20), the experiment shown in Fig. 2 can

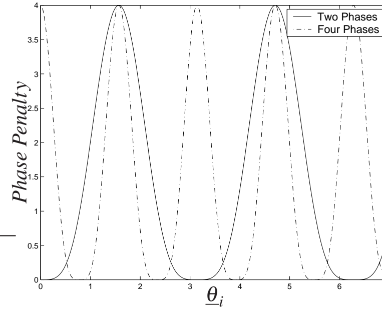


Fig. 4. Phase penalty for two-phase levels and four-phase levels

be repeated. The result is illustrated in Fig. 5. Comparison between Fig. 2 and Fig. 5 shows

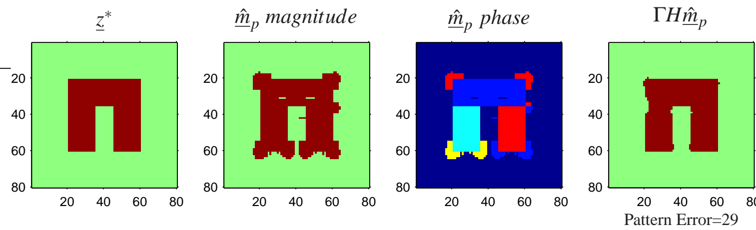


Fig. 5. Left to right: desired pattern, pole-constrained optimized mask magnitude, pole-constrained optimized mask phases (Dark blue is $\frac{\pi}{4}$, light blue is $\frac{3\pi}{4}$, yellow is $\frac{5\pi}{4}$ and red is $\frac{7\pi}{4}$) and binary output pattern. $s_{\underline{\phi}} = 2$, $s_{\underline{\theta}} = 0.01$, $\gamma_{pole,\underline{\phi}} = 0.001$ and $\gamma_{pole,\underline{\theta}} = 0.0001$.

that the pole penalty leads to fewer transmission pixels and thus fewer details in the attained mask pattern. However, some details still remain in the mask pattern. In order to remove those details, an additional penalty can be considered. The wavelet penalty regularization method is introduced next for this goal.

### *4.2. Wavelet penalty*

#### 4.2.1. Wavelet penalty

Since typical mask patterns encountered in circuitry are piecewise smooth images, the Haar wavelet is used as the building block. Consider a $N \times N$ (assume $N$ is even) image $M_{N\times N}$, where

#86458 - $15.00 USD Received 15 Aug 2007; revised 21 Sep 2007; accepted 26 Oct 2007; published 31 Oct 2007
(C) 2007 OSA

$m_{ij}$ represents the $(i,j)$ matrix element. The 1-depth Haar wavelet transform of the image above, ignoring the scale parameters, leads to the level-one approximation coefficient block and three detail coefficient blocks, each block of size $\frac{N}{2}\times\frac{N}{2}$. Specifically, the approximation coefficient block is $A_{\frac{N}{2}\times\frac{N}{2}}$, where

$$a_{ij} = m_{(2(i-1)+1)(2(j-1)+1)} + m_{(2(i-1)+1)(2(j-1)+2)} + m_{(2(i-1)+2)(2(j-1)+1)} + m_{(2(i-1)+2)(2(j-1)+2)}, \quad (23)$$

for $i,j = 1,\ldots,\frac{N}{2}$. The horizontal, vertical and diagonal detail coefficient blocks are respectively,

$$h_{ij} = m_{(2(i-1)+1)(2(j-1)+1)} - m_{(2(i-1)+1)(2(j-1)+2)} + m_{(2(i-1)+2)(2(j-1)+1)} - m_{(2(i-1)+2)(2(j-1)+2)}, \quad (24)$$

$$v_{ij} = m_{(2(i-1)+1)(2(j-1)+1)} + m_{(2(i-1)+1)(2(j-1)+2)} - m_{(2(i-1)+2)(2(j-1)+1)} - m_{(2(i-1)+2)(2(j-1)+2)}, \quad (25)$$

$$d_{ij} = m_{(2(i-1)+1)(2(j-1)+1)} - m_{(2(i-1)+1)(2(j-1)+2)} - m_{(2(i-1)+2)(2(j-1)+1)} + m_{(2(i-1)+2)(2(j-1)+2)}, \quad (26)$$

for $i,j = 1,\ldots,\frac{N}{2}$. The approximation coefficient block represents the low-frequency component of the image and the other three detail coefficient blocks represent the high-frequency components or the details of the image. Further, using Eq. (24) to Eq. (26), the total energy in the detail components is:

$$E_{detail} = \sum_{i=1}^{\frac{N}{2}} \sum_{j=1}^{\frac{N}{2}} (h_{ij}h_{ij}^* + v_{ij}v_{ij}^* + d_{ij}d_{ij}^*). \quad (27)$$

In order to remove details in the mask, the energy of the detail components should be reduced during the optimization process. Although $E_{detail}$ contains many terms, there are just three terms relative to a specific mask element $m_{ij}$. This property is convenient for calculating the energy differential of the detail components with respect to each pixel value $m_{ij}$. We refer to this property as the "localization property". The partial derivatives of $E_{detail}$ with respect to $\underline{\phi}$ and $\underline{\theta}$ are as follows [19]:

$$\begin{aligned}\frac{\partial E_{detail}}{\partial \underline{\phi}_{(2(i-1)+p)(2(j-1)+q)}} &= -\sin \underline{\phi}_{(2(i-1)+p)(2(j-1)+q)} \times Re[e^{-j\underline{\theta}_{(2(i-1)+p)(2(j-1)+q)}} \times (3\underline{m}_{(2(i-1)+p)(2(j-1)+q)} \\ &- \underline{m}_{(2(i-1)+p_1)(2(j-1)+q)} - \underline{m}_{(2(i-1)+p)(2(j-1)+q_1)} - \underline{m}_{(2(i-1)+p_1)(2(j-1)+q_1)})], \quad (28)\end{aligned}$$

$$\begin{aligned}\frac{\partial E_{detail}}{\partial \underline{\theta}_{(2(i-1)+p)(2(j-1)+q)}} &= (1+\cos \underline{\phi}_{(2(i-1)+p)(2(j-1)+q)}) \times Re[(-j)e^{-j\underline{\theta}_{(2(i-1)+p)(2(j-1)+q)}} \\ &\times (3\underline{m}_{(2(i-1)+p)(2(j-1)+q)} - \underline{m}_{(2(i-1)+p_1)(2(j-1)+q)} - \underline{m}_{(2(i-1)+p)(2(j-1)+q_1)} \\ &- \underline{m}_{(2(i-1)+p_1)(2(j-1)+q_1)})], \quad (29)\end{aligned}$$

where $i,j = 1,\ldots,\frac{N}{2}$; $p,q = 1$ *or* 2; $p_1 = (p+1)$ *mod* 2 and $q_1 = (q+1)$ *mod* 2. From Eq. (28) and Eq. (29), the gradient of $E_{detail}$ can be calculated and the cost function can be adjusted as:

$$J(\underline{m}) = F(\underline{m}) + \gamma_{pole}R_{pole}(\underline{m}) + \gamma_{wavelet}E_{detail}(\underline{m}). \quad (30)$$

The experiments of Fig. 5 are then repeated using the wavelet penalty. The results are illustrated in Fig. 6, where it can be seen that the wavelet penalty removes many small peaks at the bottom of the two parallel bars in Fig. 5. These results illustrate the efficiency of the wavelet

#86458 - $15.00 USD Received 15 Aug 2007; revised 21 Sep 2007; accepted 26 Oct 2007; published 31 Oct 2007
(C) 2007 OSA

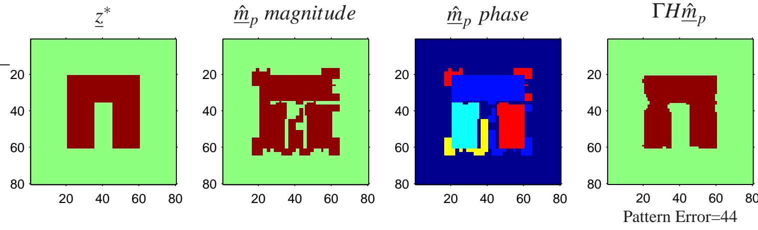


Fig. 6. Left to right: desired pattern, pole-constrained optimized mask magnitude, phase and binary output pattern. $s_{\underline{\phi}} = 2$, $s_{\underline{\theta}} = 0.01$, $\gamma_{pole,\underline{\phi}} = 0.01$, $\gamma_{pole,\underline{\theta}} = 0.001$. Wavelet regularization uses $\gamma_{wavelet,\underline{\phi}} = 0.2$ and $\gamma_{wavelet,\underline{\theta}} = 0.001$.

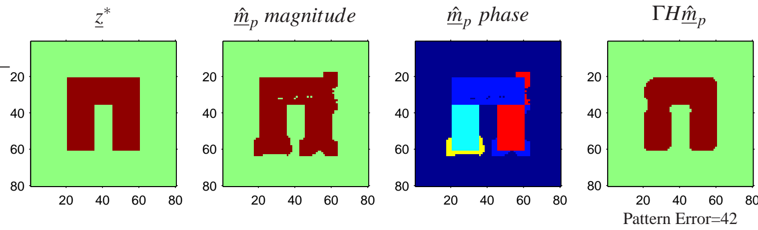


Fig. 7. Left to right: desired pattern, pole-constrained optimized mask magnitude, phase and binary output pattern. $s_{\underline{\phi}} = 2$, $s_{\underline{\theta}} = 0.01$, $\gamma_{pole,\underline{\phi}} = 0.01$, $\gamma_{pole,\underline{\theta}} = 0.001$, $\gamma_{tv,\underline{\phi}} = 0.3$ and $\gamma_{tv,\underline{\theta}} = 0.001$.

penalty. Regularization invariably will have a tradeoff reducing the pattern details while often increasing the pattern errors. Since the wavelet penalty removes small assisting blocks, the distortions of the output images are increased.

Another well-known penalty to remove details is total variation penalty. Generalized to the complex domain, the gradients of the total variation penalty are given as:

$$\nabla R_{TV}(\underline{\phi}) = [Q_x^T \operatorname{sgn}(Q_x^T \underline{f}) + Q_y^T \operatorname{sgn}(Q_y^T \underline{f})] \odot -\sin\underline{\phi} \odot Re[(\underline{m} - \underline{z}^*) \odot e^{-j\underline{\theta}}] \odot \frac{1}{2\underline{f}}, \quad (31)$$

$$\nabla R_{TV}(\underline{\theta}) = [Q_x^T \operatorname{sgn}(Q_x^T \underline{f}) + Q_y^T \operatorname{sgn}(Q_y^T \underline{f})] \odot (\underline{1} + \cos\underline{\phi}) \odot Re[(\underline{m} - \underline{z}^*) \odot e^{-j\underline{\theta}} \odot (-j)] \odot \frac{1}{2\underline{f}}, \quad (32)$$

where $\underline{f}$ is the activation pattern and $\underline{f}_j = |\underline{m}_j - \underline{z}_j^*|$ for $j = 1, \ldots, N^2$. Using the total variation penalty in our approach, the results are presented in Fig. 7. Comparing the results in Figs. 5-7, the following observations can be made. Firstly, the Haar wavelet is suitable for the piecewise smooth image. Secondly, given a set error range in the attained mask patterns in all simulations tested, the Haar wavelet penalty removes more details than the total variation penalty. Finally, the Haar wavelet penalty makes the shape of the blocks constructing the mask more regular and closer to the Haar basis functions. The Haar wavelet penalty thus leads to a set of advantages that can be attributed to the rectangular shape of the Haar basis waveforms.

### 4.2.2. Localized wavelet penalty

In the experiment above, the wavelet penalty is applied to the entire mask pattern without any local discrimination. Thus, equal penalty was assigned to details in all regions. In practice, details may be intolerable in some special mask regions, while some details may be permissible in other regions. Because of the "localization property" of the Haar wavelet penalty, we can

#86458 - \$15.00 USD Received 15 Aug 2007; revised 21 Sep 2007; accepted 26 Oct 2007; published 31 Oct 2007
(C) 2007 OSA

assign regional weights to the penalty term. Thus, a localized wavelet penalty is effective for achieving local discrimination. To this end, the cost function is adjusted as:

$$J(\underline{m}_i) = F(\underline{m}_i) + \gamma_{pole} R_{pole}(\underline{m}_i) + \omega(i)\gamma_{wavelet} E_{detail}(\underline{m}_i), \tag{33}$$

where $\omega(i),\ i = 1, \ldots N^2$ are the weight coefficients and may be changed in different spatial regions. The experimental result using localized wavelet penalty is presented in Fig. 8. The

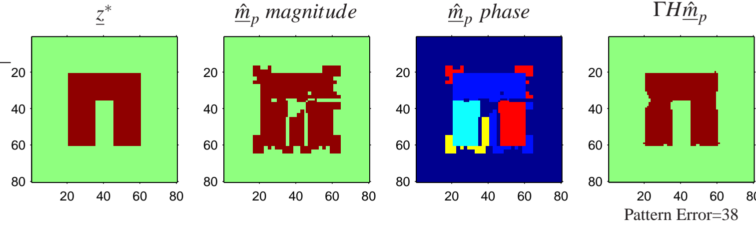


Fig. 8. Left to right: desired pattern, pole-constrained optimized mask magnitude, phase and binary output pattern. $s_{\underline{\phi}} = 2$, $s_{\underline{\theta}} = 0.01$, $\gamma_{pole,\underline{\phi}} = 0.001$, $\gamma_{pole,\underline{\theta}} = 0.0001$, $\gamma_{wavelet,\underline{\phi}} = 0.2$ and $\gamma_{wavelet,\underline{\theta}} = 0.001$. The gap between the vertical bars has regional weight of 1.6. The other regions have regional weight of 0.7.

experiment shown in Fig. 8 has the same parameters as the one shown in Fig. 6, except for the regional weights. We placed a higher cost, $\omega(i) = 1.6$, to the gap area between the vertical bars, and we assigned lower cost, $\omega(i) = 0.7$, to other regions. Comparing the results in Fig. 6 and Fig. 8, it is observed that the localized wavelet penalty removes more details in the gap, but tolerates slightly more details in other regions.

It should be noted that for some special patterns, four-phase levels are not necessary to avoid the phase assignment conflict. For instance, the parallel-bar pattern in Fig. 9 can be attained by a two-phase mask. As shown in Fig. 9, the generalized PSM algorithm is also capable of designing two-phase masks. Using the localized wavelet penalty, the attained mask design is shown in Fig. 10.

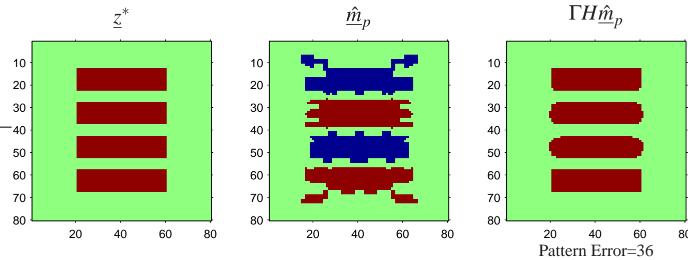


Fig. 9. Left to right: desired pattern, pole-constrained optimized mask and binary output pattern. $s_{\underline{\phi}} = 2$, $s_{\underline{\theta}} = 0.01$, $\gamma_{pole,\underline{\phi}} = 0.001$, $\gamma_{pole,\underline{\theta}} = 0.0001$, $\gamma_{wavelet,\underline{\phi}} = 0.03$ and $\gamma_{wavelet,\underline{\theta}} = 0.001$.

## 5. Double exposure optimization method

As an alternative method to the four-phase PSM, a double-exposure optimization method can be developed to avoid the phase conflict. In this method, the photoresist layer is exposed twice, each with a two-phase mask. Assume that the two masks are $M_1$ and $M_2$. Using the parametric

#86458 - $15.00 USD Received 15 Aug 2007; revised 21 Sep 2007; accepted 26 Oct 2007; published 31 Oct 2007
(C) 2007 OSA

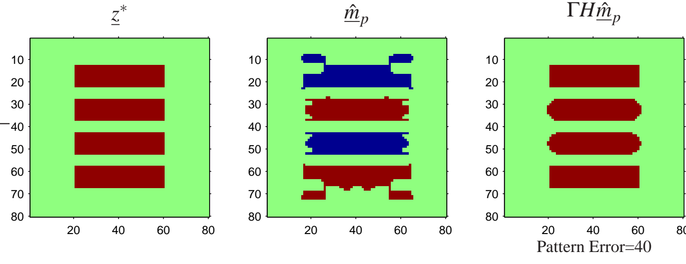


Fig. 10. Left to right: desired pattern, pole-constrained optimized mask and binary output pattern. $s_{\underline{\phi}} = 2$, $s_{\underline{\theta}} = 0.01$, $\gamma_{pole,\underline{\phi}} = 0.001$, $\gamma_{pole,\underline{\theta}} = 0.0001$, $\gamma_{wavelet,\underline{\phi}} = 0.03$ and $\gamma_{wavelet,\underline{\theta}} = 0.001$. The regions for the first and the fourth bars have regional weight of 0.8. The regions for the second and the third bars have regional weight of 1.1. The other regions have regional weight of 0.7.

transformations:

$$\underline{m}_{1k} = \underline{r}_{1k} e^{j\underline{\theta}_{1k}} = \frac{1+\cos\underline{\phi}_{1k}}{2} e^{j\underline{\theta}_{1k}}, \quad k = 1, \ldots, N^2, \tag{34}$$

$$\underline{m}_{2k} = \underline{r}_{2k} e^{j\underline{\theta}_{2k}} = \frac{1+\cos\underline{\phi}_{2k}}{2} e^{j\underline{\theta}_{2k}}, \quad k = 1, \ldots, N^2. \tag{35}$$

The corresponding output images are:

$$\underline{z}_{1k} = \frac{1}{1+\exp[-a|\sum_{k=1}^{N^2} h_{ik} \frac{1+\cos\underline{\phi}_{1k}}{2} e^{j\underline{\theta}_{1k}}| + at_r]}, \quad k = 1, \ldots, N^2, \tag{36}$$

$$\underline{z}_{2k} = \frac{1}{1+\exp[-a|\sum_{k=1}^{N^2} h_{ik} \frac{1+\cos\underline{\phi}_{2k}}{2} e^{j\underline{\theta}_{2k}}| + at_r]}, \quad k = 1, \ldots, N^2. \tag{37}$$

The superposition of $\underline{z}_1$ and $\underline{z}_2$ is the final output pattern $\underline{z}$, $\underline{z}_k = U(\underline{z}_{1k} + \underline{z}_{2k} - 1), \quad k = 1, \ldots, N^2$, where $U(\cdot)$ is a unit step function. Since the step function's derivative will introduce a Dirac impulse term that is inconvenient for further analysis, a simple approximation is given by the hyperbolic tangent function $\underline{z}_k = U(\underline{z}_{1k} + \underline{z}_{2k} - 1) \approx \frac{1}{2}[\tanh(\underline{z}_{1k} + \underline{z}_{2k} - 1) + 1], \quad k = 1, \ldots, N^2$. The cost function is then calculated as:

$$F = F(\underline{\theta}_1, \underline{\phi}_1, \underline{\theta}_2, \underline{\phi}_2) = \|\underline{z}^* - \underline{z}\|_2^2 = \sum_{i=1}^{N^2} \{z_i^* - \frac{1}{2}[\tanh(\underline{z}_{1i} + \underline{z}_{2i} - 1) + 1]\}^2. \tag{38}$$

Therefore, the gradients $\nabla F_{\underline{\theta}_1}, \nabla F_{\underline{\phi}_1}, \nabla F_{\underline{\theta}_2}$ and $\nabla F_{\underline{\phi}_2}$ can be calculated as:

$$\begin{aligned} \nabla F_{\underline{\theta}_p} &= a \times \frac{\mathbf{1} + \cos\underline{\phi}_p}{2} \odot \sin\underline{\theta}_p \odot \{H^T[(\underline{z}^* - \underline{z}) \odot \mathrm{sech}^2(\underline{z}_1 + \underline{z}_2 - \mathbf{1}) \odot \underline{z}_p \\ &\odot (\mathbf{1} - \underline{z}_p) \odot H(\underline{m}_{pR}) \odot T(\underline{m}, p)]\} \\ &- a \times \frac{\mathbf{1} + \cos\underline{\phi}_p}{2} \odot \cos\underline{\theta}_p \odot \{H^T[(\underline{z}^* - \underline{z}) \odot \mathrm{sech}^2(\underline{z}_1 + \underline{z}_2 - \mathbf{1}) \odot \underline{z}_p \\ &\odot (\mathbf{1} - \underline{z})_p \odot H(\underline{m}_{pI}) \odot T(\underline{m}, p)]\}, \end{aligned} \tag{39}$$

#86458 - $15.00 USD Received 15 Aug 2007; revised 21 Sep 2007; accepted 26 Oct 2007; published 31 Oct 2007
(C) 2007 OSA

$$
\begin{aligned}
\nabla F_{\underline{\phi}_p} &= \frac{a}{2} \times \sin \underline{\phi}_p \odot \cos \underline{\theta}_p \odot \{H^T[(\underline{z}^* - \underline{z}) \odot \text{sech}^2(\underline{z}_1 + \underline{z}_2 - \mathbf{\underline{1}}) \odot \underline{z}_p \\
&\odot \quad (\mathbf{\underline{1}} - \underline{z}_p) \odot H(\underline{m}_{pR}) \odot T(\underline{m}, p)]\} \\
&+ \quad \frac{a}{2} \times \sin \underline{\phi}_p \odot \sin \underline{\theta}_p \odot \{H^T[(\underline{z}^* - \underline{z}) \odot \text{sech}^2(\underline{z}_1 + \underline{z}_2 - \mathbf{\underline{1}}) \odot \underline{z}_p \\
&\odot \quad (\mathbf{\underline{1}} - \underline{z}_p) \odot H(\underline{m}_{pI}) \odot T(\underline{m}, p)]\},
\end{aligned} \tag{40}
$$

where $p = 1$ *or* 2 and $T(\underline{m}, p) = [H(\underline{m}_{pR})^2 + H(\underline{m}_{pI})^2]^{-\frac{1}{2}}$. Both pole penalty and wavelet penalty can be applied to the double-exposure optimization method. The experiment shown in Fig. 2 is repeated in Fig. 11, where a double-exposure method is used. It is obvious that the pattern error is effectively reduced. The double-exposure optimization method is indeed effective, but requires more complicated processing and longer fabrication time. As mentioned in the introduction, independently from our work, Poonawala and Milanfar have developed a double-exposure inverse lithography method. Although similar in concept, these two approaches are different. Their method optimizes the inverse lithography process prior to a threshold operator, whereas the double-exposure method presented in this paper encompasses the threshold operator that models the photoresist development stage.

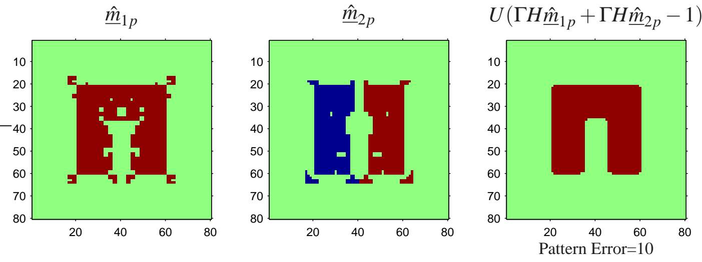


Fig. 11. Left to right: mask for first exposure, mask for second exposure and the output pattern. $s_{\underline{\phi}_1} = 4$, $s_{\underline{\theta}_1} = 0.01$, $s_{\underline{\phi}_2} = 4$, $s_{\underline{\theta}_2} = 0.01$, $\gamma_{pole,\underline{\phi}_1} = 0.015$, $\gamma_{pole,\underline{\theta}_1} = 0.001$, $\gamma_{wavelet,\underline{\phi}_1} = 0.5$, $\gamma_{wavelet,\underline{\theta}_1} = 0.003$, $\gamma_{pole,\underline{\phi}_2} = 0.015$, $\gamma_{pole,\underline{\theta}_2} = 0.001$, $\gamma_{wavelet,\underline{\phi}_2} = 0.5$ and $\gamma_{wavelet,\underline{\theta}_2} = 0.003$.

## 6. Conclusion

This paper studies and models the optical system for generalized inverse lithography. A pixel-based mask representation is used and the MSE between the output pattern and the desired pattern is used to measure the pattern error. The cost function approach used enables the algorithm to search for a solution in the entire complex plane, and as such avoiding possible phase conflicts. In order to control the amount of details, the pole penalty terms are used to curb the transmission regions on the mask pattern and constrain the phases to several prescribed discrete levels. Another contribution of this paper is the introduction of the wavelet penalty used to reduce the mask complexity. Because of the "localization property", regional weighting can be applied to different areas on the mask pattern. Finally, a double-exposure optimization method is introduced. It is capable to avoid the phase conflict and results in much less pattern error as well.

#86458 - $15.00 USD Received 15 Aug 2007; revised 21 Sep 2007; accepted 26 Oct 2007; published 31 Oct 2007
(C) 2007 OSA